

Generation of bright phase-matched circularly-polarized extreme ultraviolet high harmonics

Ofer Kfir^{1*}, Patrik Grychtol², Emrah Turgut², Ronny Knut^{2,3}, Dmitriy Zusin², Dimitar Popmintchev², Tenio Popmintchev², Hans Nembach^{2,3}, Justin M. Shaw³, Avner Fleischer^{1,4}, Henry Kapteyn², Margaret Murnane² and Oren Cohen^{1*}

Circularly-polarized extreme ultraviolet and X-ray radiation is useful for analysing the structural, electronic and magnetic properties of materials. To date, such radiation has only been available at large-scale X-ray facilities such as synchrotrons. Here, we demonstrate the first bright, phase-matched, extreme ultraviolet circularly-polarized high harmonics source. The harmonics are emitted when bi-chromatic counter-rotating circularly-polarized laser pulses field-ionize a gas in a hollow-core waveguide. We use this new light source for magnetic circular dichroism measurements at the *M*-shell absorption edges of Co. We show that phase-matching of circularly-polarized harmonics is unique and robust, producing a photon flux comparable to linearly polarized high harmonic sources. This work represents a critical advance towards the development of table-top systems for element-specific imaging and spectroscopy of multiple elements simultaneously in magnetic and other chiral media with very high spatial and temporal resolution.

Circularly-polarized radiation in the extreme ultraviolet (EUV) and soft X-ray spectral regions has proven to be extremely useful for investigating chirality-sensitive light-matter interactions. It enables studies of chiral molecules using photoelectron circular dichroism¹, ultrafast molecular decay dynamics², the direct measurement of quantum phases (for example, Berry's phase and pseudo-spin) in graphene and topological insulators^{3,4} and reconstruction of band structure and modal phases in solids⁵. For magnetic materials, circularly-polarized soft X-rays are particularly useful for X-ray magnetic circular dichroism (XMCD) spectroscopy⁶, which enables element-selective probing as well as coherent imaging and holography of magnetic structures with nanometre resolution^{7–9}. XMCD can also be used to extract detailed information about the magnetic state by distinguishing between the spin and orbital magnetic moments of each element. Thus, time-resolved XMCD can probe the element-specific dynamics of the spin and orbital moments when interacting with the electronic and phononic degrees of freedom in a material^{10,11}. Although ultrafast magnetic dynamics has been studied for 20 years¹², the time resolution of XMCD remains >100 fs, limited by the pulse duration and timing jitter of synchrotron and free-electron laser pulses^{13,14}. To date, it has not been possible to simultaneously probe the spin dynamics of multiple elements within a single sample, because the photon energy must be tuned across the various absorption edges at large-scale facilities (where these experiments are currently performed).

Table-top soft X-ray sources based on high harmonic upconversion of femtosecond laser pulses represent a viable alternative to large-scale sources for many applications, due to their unique ability to generate bright, broadband, ultrashort and coherent light with an energy spectrum reaching into the keV region¹⁵. High harmonic generation (HHG) not only enables coherent imaging of nanometre structures with a spatial resolution approaching the diffraction limit¹⁶, but also accesses the fastest dynamics in

atoms, molecules, solids and plasmas with unprecedented time resolution^{17–23}. The large bandwidth and short temporal duration of HHG makes it a versatile, element-specific probe of coupled spin, charge and phonon dynamics on ultrafast timescales. In the case of magnetic materials, recent work has shown that HHG can simultaneously probe the magnetic state of the 3*d* ferromagnets Fe, Co and Ni by taking advantage of the fact that the reflectivity near the *M*-shell absorption edges depends on the orientation as well as the magnitude of the magnetization²⁴. This novel capability has made it possible to gain a new fundamental understanding about the timescale of the exchange interaction, as well as revealing the important roles of local spin scattering and non-local spin transport, all of which can occur on few-femtosecond timescales^{25,26}. The vast majority of HHG applications to date, however, have used linearly polarized light, which can be generated relatively efficiently.

For decades it was generally assumed that HHG from atoms is bright when both the driving laser and HHG fields are linearly polarized. The source of this misconception is that HHG is a re-collision phenomenon. A bound electron is ripped from an atom by the intense electric field of a driving laser pulse and then accelerated as a free electron until it re-encounters its parent ion²⁷. For a linearly polarized driving field, the electron accelerates on a linear trajectory, and therefore easily re-collides with the parent ion. When driven by a slightly elliptical laser field, the electron has some probability of re-colliding with its parent ion due to lateral spreading (quantum diffusion) of the wavefunction in the continuum²⁸. This results in the generation of slightly elliptically polarized high harmonics²⁹. In contrast, for circularly-polarized driving lasers (or elliptically-polarized lasers with a large ellipticity), the probability of re-collision and the emission of high harmonics is completely suppressed. Nevertheless, because of important applications in materials science, there was strong motivation to generate bright circularly-polarized high harmonic beams^{30–40}. The first experimentally measured circularly-polarized high-order harmonics were produced by

¹Solid State Institute and Physics Department, Technion, Haifa 32000, Israel. ²Department of Physics and JILA, University of Colorado and NIST, Boulder, Colorado 80309, USA. ³Electromagnetics Division, National Institute of Standards and Technology, Boulder, Colorado 80305, USA. ⁴Department of Physics and Optical Engineering, Ort Braude College, Karmiel 21982, Israel. *e-mail: ofertx@technion.ac.il; oren@technion.ac.il

Report Documentation Page				Form Approved OMB No. 0704-0188	
Public reporting burden for the collection of information is estimated to average 1 hour per response, including the time for reviewing instructions, searching existing data sources, gathering and maintaining the data needed, and completing and reviewing the collection of information. Send comments regarding this burden estimate or any other aspect of this collection of information, including suggestions for reducing this burden, to Washington Headquarters Services, Directorate for Information Operations and Reports, 1215 Jefferson Davis Highway, Suite 1204, Arlington VA 22202-4302. Respondents should be aware that notwithstanding any other provision of law, no person shall be subject to a penalty for failing to comply with a collection of information if it does not display a currently valid OMB control number.					
1. REPORT DATE 08 DEC 2014		2. REPORT TYPE		3. DATES COVERED 00-00-2014 to 00-00-2014	
4. TITLE AND SUBTITLE Generation of Bright Phase-matched Circularly-polarized Extreme Ultraviolet High Harmonics				5a. CONTRACT NUMBER	
				5b. GRANT NUMBER	
				5c. PROGRAM ELEMENT NUMBER	
6. AUTHOR(S)				5d. PROJECT NUMBER	
				5e. TASK NUMBER	
				5f. WORK UNIT NUMBER	
7. PERFORMING ORGANIZATION NAME(S) AND ADDRESS(ES) University of Colorado, Boulder,JILA and Department of Physics,Boulder,CO,80309				8. PERFORMING ORGANIZATION REPORT NUMBER	
9. SPONSORING/MONITORING AGENCY NAME(S) AND ADDRESS(ES)				10. SPONSOR/MONITOR'S ACRONYM(S)	
				11. SPONSOR/MONITOR'S REPORT NUMBER(S)	
12. DISTRIBUTION/AVAILABILITY STATEMENT Approved for public release; distribution unlimited					
13. SUPPLEMENTARY NOTES					
14. ABSTRACT					
15. SUBJECT TERMS					
16. SECURITY CLASSIFICATION OF:			17. LIMITATION OF ABSTRACT Same as Report (SAR)	18. NUMBER OF PAGES 16	19a. NAME OF RESPONSIBLE PERSON
a. REPORT unclassified	b. ABSTRACT unclassified	c. THIS PAGE unclassified			

converting the polarization of linearly polarized HHG to circular, using a reflective quarter-waveplate³³. This approach is very lossy, is limited to narrow spectral regions constrained by the available multi-layer mirror materials, and to date has not proven useful for applications. A direct approach for generating circularly-polarized HHG was suggested almost two decades ago^{41,42} and recently measured by Fleischer and colleagues⁴³. In this scheme, circularly-polarized high harmonics are driven by co-propagating circularly-polarized bi-chromatic fields that rotate in opposite directions and interact with an isotropic gas. Notably, Fleischer and co-workers measured the ellipticity of weak harmonics generated from HHG in a thin gas jet, but not their helicity (that is, right- versus left-circular polarization).

In this Article we generate bright, phase-matched, circularly-polarized high harmonic beams for the first time, and then use this unique light source to implement the first table-top XMCD measurements. To achieve this, we first demonstrate (both experimentally and theoretically) that phase-matching of high harmonics driven by circularly polarized bi-chromatic waves differs significantly from all other approaches to phase-matching to date. Phase-matching is more robust for HHG with bi-chromatic linearly- or elliptically-polarized drivers. Moreover, phase-matching can selectively enhance either left or right circularly-polarized harmonics, a critical feature for generating circularly-polarized attosecond pulses. Using this new understanding, we generate bright circularly-polarized high harmonics by co-propagating bi-chromatic driving laser beams (the fundamental and second-harmonic beams from a Ti:sapphire laser) that are circularly-polarized with opposite helicity in a gas-filled hollow waveguide (see Supplementary Section 6 for details on the important features of this source). We show that bright, circularly-polarized, high harmonics in Ne can span multiple M -edges of the $3d$ ferromagnets, and obtain a photon flux of $\sim 1 \times 10^9$ HHG photons per second per harmonic (Supplementary Section 5), which is comparable to the linearly-polarized HHG flux that was used very successfully in previous ultrafast element-selective magneto-optic HHG-based experiments^{24–26}. Finally, we measure the circular dichroism of Co throughout the M -shell absorption edge spectral region. This measurement is also the first to measure the helicity of circularly-polarized high-order harmonic beams. In the future, the use of mid-infrared pump lasers should make it possible to generate bright circularly-polarized high harmonics at the L -shell absorption edges of Fe, Co and Ni, in a photon energy range approaching 1 keV (ref. 15).

Phase-matching of circularly-polarized HHG

We first describe the theoretical spectral and polarization features of our source driven by a left-rotating circularly-polarized fundamental beam at a central wavelength of 790 nm, and a right-rotating circularly-polarized second-harmonic beam (Fig. 1a). We consider an idealized case in which the medium is isotropic and time-independent, and where the driving laser is perfectly periodic. Independently of the relative intensity or phase between the two pump fields, the bi-chromatic field, $\mathbf{E}_{BC}(t)$, exhibits the following dynamical symmetry: $\mathbf{E}_{BC}(t + T/3) = \hat{R}_{(120^\circ)} \mathbf{E}_{BC}(t)$. T is the optical cycle of the fundamental laser and $\hat{R}_{(120^\circ)}$ is the 120° rotation operator in the polarization plane. The emitted HHG field conforms to the same dynamical symmetry³⁰. Thus, as can be verified by taking the Fourier transform of the dynamical symmetry constraint, the complex amplitude of each q th-order harmonic, \mathbf{E}_q , satisfies the following eigenvalue equation

$$\mathbf{E}_q e^{-2\pi i q/3} = \hat{R}_{(120^\circ)} \mathbf{E}_q \quad (1)$$

The solutions of equation (1) are a left circularly-polarized field with eigenvalue $e^{-2\pi i/3}$ and a right circularly-polarized field with eigenvalue $e^{+2\pi i/3}$. The left circularly-polarized q th-order harmonic,

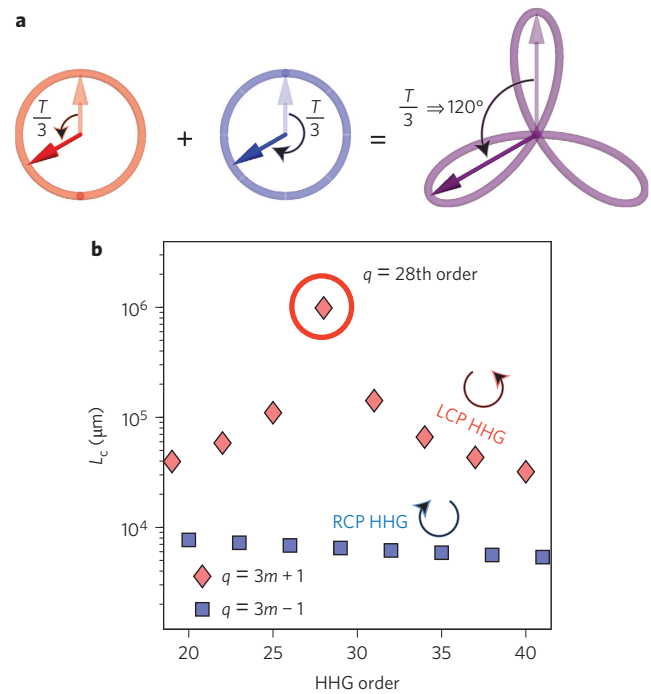


Figure 1 | Pump symmetry and phase-matching condition for circularly-polarized HHG.

a, The combined electric field of a left-circularly-polarized 790 nm driving laser beam (red) and a counter-rotating second-harmonic field (blue) is a threefold rosette shape (purple). The system has a discrete rotation dynamical symmetry of the light field, where a delay of $T/3$ acts as a 120° rotation. This dynamical symmetry gives rise to circularly-polarized harmonics where harmonic orders $q = 3m - 1$ rotate right and $q = 3m + 1$ rotate left. **b**, Calculated coherence length versus HHG order under phase-matching conditions that optimize the 28th harmonic. Phase-matching of circularly-polarized HHG is helicity-selective, so HHG orders $q = 3m + 1$ (left-circular polarization, LCP) have a longer coherence length (better phase-matching) than $q = 3m - 1$ (right-circular polarization, RCP). Reabsorption of high harmonics in the gas medium reduces the contrast arising from this effect, as detailed in Supplementary Section 1.

$\mathbf{E}_{q,L}$, satisfies $e^{-(2\pi i q/3)} \mathbf{E}_{q,L} = e^{-(2\pi i/3)} \mathbf{E}_{q,L}$, which is fulfilled only when $q = 3m + 1$. Similarly, the right circularly-polarized q th-order harmonic, $\mathbf{E}_{q,R}$, satisfies $e^{-(2\pi i q/3)} \mathbf{E}_{q,R} = e^{+(2\pi i/3)} \mathbf{E}_{q,R}$, which is fulfilled only when $q = 3m - 1$. Notably, $q = 3m$ harmonics do not satisfy equation (1) and are therefore theoretically forbidden.

Phase-matching is essential for obtaining a bright and collimated high harmonic beam. In HHG with linearly-polarized bi-chromatic drivers, the phases and intensities of the emitted harmonics depend strongly on the relative phase between the chromatic drivers, due to the intrinsic phases of the rescattering electrons⁴⁴. Consequentially, full phase-matching in this case requires that the two driver fields and the harmonic field propagate at the same phase velocity, a very challenging condition to satisfy. Fortunately, phase-matching of HHG driven by circularly-polarized bi-chromatic drivers is very different. In this case, the relative phase between the chromatic driver components does not influence the shape (rosette) of the bi-chromatic driver (see Supplementary Movie), and hence it also does not influence the path length of the re-colliding electron and the intrinsic phase it accumulates. Thus, phase mismatch of the process is determined only by the extrinsic phase, and is described by the ‘ordinary’ phase-mismatch equation in nonlinear optics:

$$\frac{\pi}{L_c} = \Delta k = k_q - \ell k_1 - m k_2 \quad (2)$$

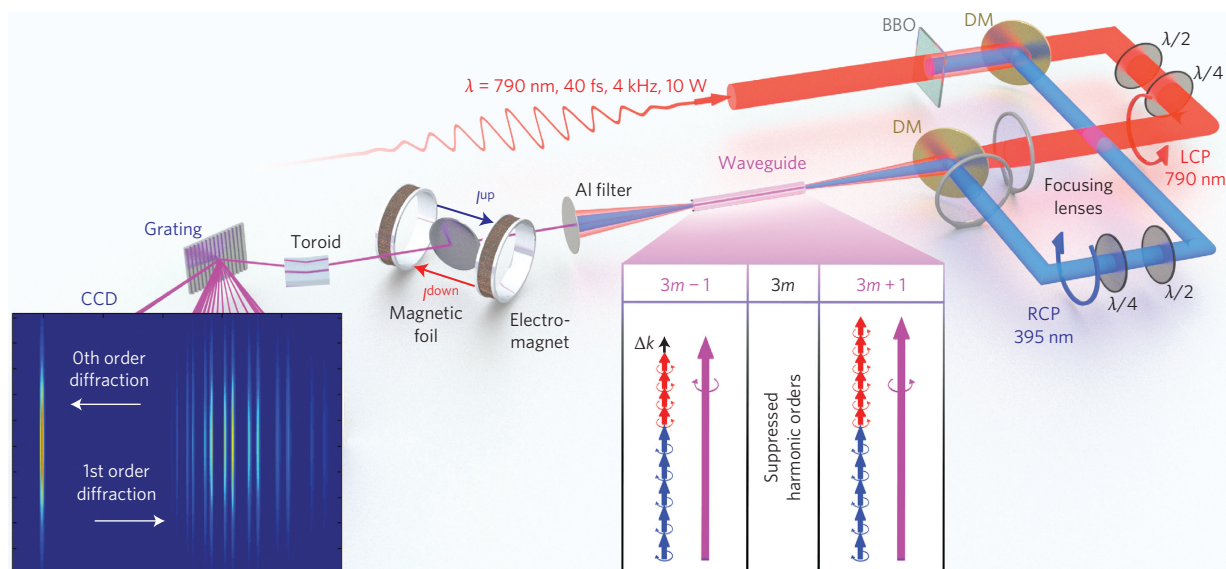


Figure 2 | Experimental apparatus. Circularly-polarized harmonics are generated by focusing fundamental and second-harmonic pump beams (with opposing helicities) into a gas-filled hollow waveguide. The polarization states of the two drivers can be adjusted independently, thereby controlling the helicity of the generated harmonics. The magnetic state of a sample can then be measured with elemental specificity via XMCD by using harmonics that overlap with an appropriate core-level absorption edge, for example, the *M*-edge of Co. Right inset: helicity selectiveness for phase-matching of circularly-polarized HHG, where left-rotating harmonics ($q = 3m + 1$) and right-rotating harmonics ($q = 3m - 1$) cannot be phase-matched simultaneously. In other words, if the $q = 3m + 1$ harmonics are phase-matched with the pump lasers, then the $q = 3m - 1$ harmonics are mismatched by Δk . Left inset: typical experimental spectrum recorded on the CCD.

where k_q , k_1 and k_2 are the wavevectors for the q th-order high-harmonic, fundamental and second harmonic beams, respectively, Δk is the phase mismatch of the upconversion process, and L_c is the resulting coherence length. ℓ and m are the number of photons of the fundamental and second-harmonic pump beams, respectively, converted to a q th-order high harmonic photon. Conservation of energy and angular momentum impose that $q = \ell + 2m$, and $\ell = m \pm 1$, respectively⁴³. These conservations imply that left (right) circularly-polarized harmonics are generated from a combination of m second-harmonic photons and $m + 1$ ($m - 1$) fundamental photons.

For simplicity, we associate k_1 and k_2 with the effective index change, Δn_1 and Δn_2 , respectively, defined as $\Delta n_i = (k_i/[2\pi/\lambda_i] - 1)$, where λ_i is the vacuum wavelength of the i th driver ($i = 1$ for the fundamental pump and $i = 2$ for the second-harmonic pump). Thus, we can rewrite equation (2) in the form:

$$\frac{\pi}{L_c} = -\frac{2\pi}{\lambda_1} [m(\Delta n_1 + 2\Delta n_2) \pm \Delta n_1] \quad (3)$$

where the + and - signs correspond to the $q = 3m + 1$ and $q = 3m - 1$ groups of harmonics, respectively. The factor $\pm \Delta n_1$ leads to a large difference in the coherence lengths between the combs of left and right rotating circular harmonics. Physically, this difference reflects the different ratios between the fundamental and second-harmonic photons, $(m + 1)/m$ and $(m - 1)/m$, which participate in the generation of left and right circularly-polarized harmonics, respectively.

Figure 1b presents numerical results for the phase-matching of circularly-polarized HHG. The coherence lengths shown in Fig. 1b are calculated for Δn_1 and Δn_2 that optimize phase-matching for the 28th harmonic. As expected, the $q = 3m + 1$ harmonics are brighter (i.e. better phase-matched to the bi-chromatic pump) than the harmonics with opposite helicity. Notably, to implement phase-matched HHG frequency upconversion, the ionization level of the gas must be below a critical value, η_{cr} (ref. 45). For HHG with a circularly polarized bi-chromatic driver, η_{cr} has a value

between the critical ionization for HHG driven by the fundamental or second harmonic, separately (Supplementary equation (S.3)). This also results in a phase-matching cutoff photon energy that is somewhere between the cutoff corresponding to the fundamental and second harmonic, separately. Finally, we note that our model does not include the HHG intensity-dependent phase, through which the temporal envelope of the pump pulse affects the instantaneous phase mismatch. However, the dependence of the harmonic phase on the intensity of the bi-chromatic pump laser is weak³⁸.

Figure 2 presents a schematic of the experimental apparatus. A Ti:sapphire oscillator is used in combination with a single-stage regenerative amplifier, delivering sub-45 fs pulses at a repetition rate of 4 kHz, which are centred at a wavelength of 790 nm (red), with an energy of 2.5 mJ per pulse. After frequency-doubling the laser beam in a β -phase barium borate (BBO) crystal, the bi-chromatic co-propagating driving fields are separated by a dichroic mirror (DM) into two different arms of a Mach-Zehnder interferometer. An optical delay stage in the red arm compensates for the relative time delay between the two colours, and the polarization of each arm is fully controlled by a pair of half- and quarter-wavelength retardation plates. The red (1.6 mJ/pulse) and blue (0.43 mJ/pulse) driving lasers are focused into a 150- μ m-diameter, 2-cm-long gas-filled hollow waveguide using lenses with focal lengths of 50 cm and 75 cm, respectively. The circularly-polarized HHG beam that emerges from the waveguide then passes through an Al filter to block the pump laser beams. In the first experiment, the HHG beam was spectrally dispersed using a spectrometer composed of a toroidal mirror, a laminar Au grating with a groove density of 500 lines/mm and a charge-coupled device (CCD) camera. In the second experiment, the HHG beam passed through a magnetized 100-nm-thick Co foil tilted by 45° with respect to the harmonics beam before entering the spectrometer. The magnetization of the Co foil was controlled by an external electromagnet that produced a magnetic field of $\sim 4.8 \times 10^4$ A m⁻¹ (60 mT) parallel to the sample plane, exceeding the 1.6×10^4 A m⁻¹ (20 mT) coercive field of the foil. The alternating polarity of the

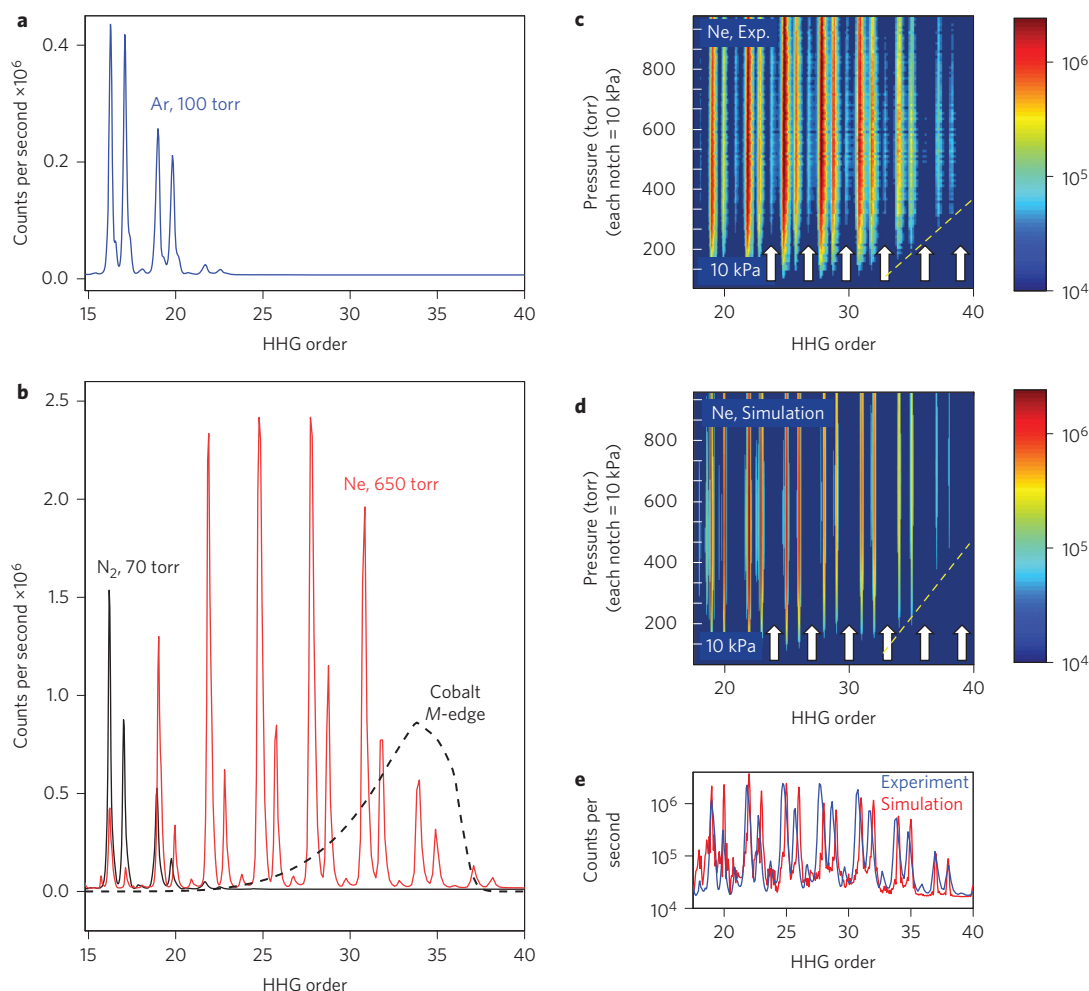


Figure 3 | Generation of bright circularly-polarized harmonics. **a**, HHG spectrum from Ar. **b**, HHG from N₂ at 70 torr (black) and Ne at 650 torr (red). The HHG spectrum for Ne covers the Co M-edge (black dashed curve⁴⁷). The circular polarization of the HHG is manifested by suppression of the 3 m harmonics (15, 18, ..., white arrows in **c** and **d**). **c**, Colour-coded experimental (**c**) and simulated (**d**) pressure-dependent spectrograms of HHG with Ne. Each notch mark on left axes indicates 10 kPa. Colour coding in **c** is a logarithm of the photoelectron counts per second on the CCD. The experimental and theoretical spectrograms exhibit a known feature of phase-matching in Ne: higher-order harmonics are phase-matched through a narrower pressure range than lower-order harmonics (dashed lines guide the eye). **e**, Measured (solid blue line) and normalized simulated (dashed red line) spectra (on a log scale) with 650 torr of Ne.

magnet was synchronized to the spectrometer readout, so that we were able to acquire the transmitted HHG spectrum for two ('up' and 'down') magnetization directions. The normalized difference of these two spectra constitutes the XMCD asymmetry. Positioning the ferromagnetic sample at 45° to the HHG beam allowed observation of XMCD of a sample magnetized in plane⁴⁶.

We first discuss the brightness, spectrum and polarization of the EUV light produced by this novel HHG source. Figure 3a presents the observed HHG spectrum when the hollow waveguide was filled with Ar gas at a pressure of 100 torr (13 kPa), with the driving laser beams blocked by Al filters of ~800 nm thickness. Figure 3b displays the observed HHG spectra from 650 torr (87 kPa) of Ne and 70 torr (9 kPa) of N₂ using 400-nm-thick Al filters. Clearly, the $q = 3m$ harmonics are almost completely suppressed over the entire observed HHG spectra for all gas species. This feature indicates that the polarization of the harmonics is nearly circular⁴³.

Figure 3c and 3d, present, respectively, experimental and simulated pressure-dependent spectrograms of HHG emission from a Ne-filled hollow waveguide (see Supplementary Section 3 for details). Two features are worth mentioning. First, the 3 m HHG orders are suppressed throughout the pressure range, reflecting the

single-atom dynamical symmetry described in equation (1). Second, the intensity of the plateau harmonics dramatically increases at pressures above 100 torr (13 kPa), indicating that they are phase-matched throughout this pressure range. However, the cutoff harmonics are phase-matched within a narrower pressure range, as marked by yellow dashed lines. This effect, which also exists in HHG from linearly-polarized driving fields⁴⁵, results from two complementary effects. First, a larger effective index change, $|\Delta n_1|$, $|\Delta n_2|$, is required for phase-matching higher-order HHG. Thus, deviation from perfect phase-matching in equation (2), say 1% of $\Delta n_{1,2}$, affects the absolute value of the coherence length L_c more drastically. Second, the longer reabsorption length of higher HHG orders in Ne⁴⁷ makes the phase-matched throughput even more sensitive to imperfect phase-matching conditions. Notably, reabsorption of the high harmonics in Ne limits the distinction between full and partial phase-matching. Therefore, the output flux contrast between one perfectly phase-matched harmonic (e.g. 28th order in Fig. 1b) and the rest of the 3 $m + 1$ harmonic orders is insignificant. Most importantly, the current flux of circularly-polarized photons produced by our scheme is sufficient for application experiments such as XMCD, as described in the following section.

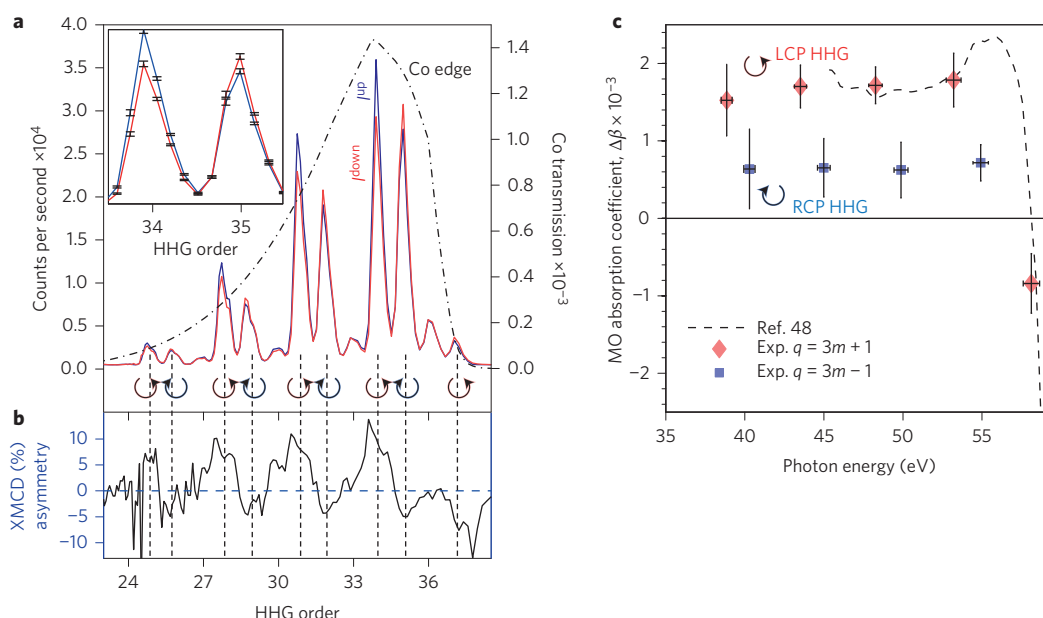


Figure 4 | Co XMCD. **a**, Spectra of circularly-polarized HHG transmitted through 100 nm of magnetized Co with the magnetization direction either ‘up’ (I^{up} , blue) or ‘down’ (I^{down} , red). The dashed black envelope shows the transmission spectrum of Co (units along the right axis)⁴⁷. Inset: difference in signal between ‘up’ and ‘down’ magnetization for the 34th and 35th orders, including experimental error. Round arrows indicate HHG helicity. **b**, Experimental XMCD asymmetry defined by $(I^{\text{up}} - I^{\text{down}})/(I^{\text{up}} + I^{\text{down}})$. The alternating asymmetry for adjacent harmonics is consistent with the prediction of alternating harmonic helicity. **c**, Magneto-optical (MO) absorption coefficient $\Delta\beta$, derived from XMCD asymmetry of the $3m + 1$ (red diamonds) and $3m - 1$ (blue squares) harmonics. The experimental MO coefficient derived from the $3m + 1$ harmonics accurately retrieves literature MO values (dashed line) without fitting any parameters. The reduced intensities and XMCD asymmetry of the $3m - 1$ harmonics suggests that these harmonics have lower ellipticity.

Magnetic circular dichroism

To demonstrate the utility of this table-top HHG source with circularly-polarized EUV light for probing magnetization, we measured XMCD of a freestanding thin Co foil. The imaginary (that is, absorptive) part of the refractive index n for light propagating in a magnetically saturated film is given by $\text{Im}[n] = \beta \pm \Delta\beta$ where β is the average absorption coefficient and $\Delta\beta$ is the dichroic absorption coefficient for circularly-polarized light, where the (\pm) marks the absorption difference for left- versus right-circularly polarized EUV photons^{46,48}. The dichroic absorption scales linearly with the component of the magnetization parallel to the direction of light propagation. For example, the absorption coefficient of a sample with magnetization M that is below its saturation value M_{sat} , pointing at angle θ with respect to the beam direction, is $(M/M_{\text{sat}}) \cos \theta \cdot \Delta\beta$. However, XMCD requires a bright circularly-polarized soft X-ray source, because the non-dichroic absorption coefficient is approximately ten times larger than the dichroic coefficient, leading to strong average absorption that far exceeds the dichroic signal.

We measured the HHG spectrum after passing through a magnetized Co foil, as shown in Figs 2 and 4. Figure 4a presents the transmitted spectrum, I^{up} and I^{down} , for ‘up’ and ‘down’ Co magnetization, respectively. The normalized XMCD asymmetry, $A = (I^{\text{up}} - I^{\text{down}})/(I^{\text{up}} + I^{\text{down}})$ is shown in Fig. 4b. The asymmetry of the $3m + 1$ and $3m - 1$ harmonics exhibits opposite signs, proving that the helicity of the $3m + 1$ harmonics is indeed opposite to that of the $3m - 1$ harmonics.

Finally, we used the measured XMCD asymmetry to extract the magneto-optical (MO) dichroic absorption coefficient, $\Delta\beta$, for Co. The MO dichroic absorption coefficient is given by $\Delta\beta = \tanh^{-1}(A)/(2|k_0| \cos \theta L)$, where k_0 is the light wavevector, L is the optical path length in the sample and θ is the angle between the sample magnetization and beam propagation direction⁴⁶. Because the sample magnetization is tilted by 45° , the optical path is $\sqrt{2}$ times the sample thickness d , and $\cos \theta = 1/\sqrt{2}$, the MO

dichroic coefficient is simply $\Delta\beta = \tanh^{-1}(A)/(2|k_0|d)$. Our results for $\Delta\beta$ are presented in Fig. 4c. For each HHG order, we estimate $\Delta\beta$ from a weighted average over a harmonic peak, without any adjustable fitting parameters, where the error bars are the standard deviation over the same harmonic. The MO coefficient measured by the left circularly-polarized $3m + 1$ harmonics matches measurements that were taken using synchrotrons⁴⁸, indicating that their polarization is circular (see Supplementary Section 7 for quantitative analysis of Stokes parameter). However, the low intensity and low MO dichroic absorption coefficient measured using the right circularly-polarized 29th, 32nd and 35th harmonics (corresponding to the $3m - 1$ group) at 45 eV, 50 eV and 55 eV, respectively, indicate that their polarization is elliptical with an ellipticity of ~ 0.2 . We associate the asymmetry between the right and left high harmonics with the fact that the rosette-shape bi-chromatic driving laser induces electronic rotating current in the atoms, influencing both the single-atom HHG process⁴⁹ and HHG re-absorption. Interestingly, the XMCD measurement also shows that the polarization of the significantly suppressed $3m$ harmonics is also chiral, with the same helicity as the $3m + 1$ harmonics. This observation agrees with the numerical calculations presented in ref. 43 (Figs 3c and 3f), where the polarizations of the bi-chromatic drivers deviate from perfect circularity.

Conclusions and outlook

We have demonstrated the first bright, phase-matched source of circularly-polarized high harmonics and also the first M -edge X-ray magnetic circular dichroism measurements of magnetic materials on a table top. Our HHG source produces a broad spectrum of bright circularly-polarized harmonics, where consecutive harmonics exhibit opposite helicity, and where phase-matching considerations are robust and favour one helicity over the other. This work removes a major constraint to date—that the polarization of bright high harmonics sources is limited to linear polarization—and therefore paves the way for ultrafast circular dichroism studies of

magnetism, chiral molecules and nanostructures, as well as for exploring the interaction of atoms with chiral EUV fields. In combination with coherent diffraction imaging techniques, this advancement will also enable the exploration of coupled spin, charge and structural dynamics of magnetic domains with elemental specificity and unprecedented spatial and temporal resolution. The temporal resolution of a measurement using a single harmonic from our system would be in the range of 45 fs (determined by the pump and the harmonic bandwidth). To access the attosecond regime in chiral experiments, interaction with several helical harmonics that rotate in the same direction (and therefore form a helical attosecond pulse train) is required. The chirality-selective phase-matching can very nicely enhance only harmonics with a specific helicity, thereby producing circularly-polarized attosecond pulses. Our source might also be used for seeding X-ray free-electron lasers to obtain ultra-bright circularly-polarized X-rays⁵⁰. Finally, the scheme we use is universal, and can be used to generate circularly-polarized high harmonics across very broad spectral regions, for example, through quasi phase-matching of the HHG process, by using mid-infrared driving lasers¹⁵ or by using other nonlinear media.

Received 18 April 2014; accepted 30 October 2014;
published online 8 December 2014

References

- Böwring, N. *et al.* Asymmetry in photoelectron emission from chiral molecules induced by circularly polarized light. *Phys. Rev. Lett.* **86**, 1187–1190 (2001).
- Travnikova, O. *et al.* Circularly polarized X rays: another probe of ultrafast molecular decay dynamics. *Phys. Rev. Lett.* **105**, 233001 (2010).
- Gierz, I., Lindroos, M., Höchst, H., Ast, C. R. & Kern, K. Graphene sublattice symmetry and isospin determined by circular dichroism in angle-resolved photoemission spectroscopy. *Nano Lett.* **12**, 3900–3904 (2012).
- Xu, S.-Y. *et al.* Hedgehog spin texture and Berry's phase tuning in a magnetic topological insulator. *Nature Phys.* **8**, 616–622 (2012).
- Liu, Y., Bian, G., Miller, T. & Chiang, T.-C. Visualizing electronic chirality and Berry phases in graphene systems using photoemission with circularly polarized light. *Phys. Rev. Lett.* **107**, 166803 (2011).
- Schütz, G., Knülle, M. & Ebert, H. Magnetic circular X-ray dichroism and its relation to local moments. *Phys. Scr.* **1993**, 302 (1993).
- Stöhr, J. *et al.* Element-specific magnetic microscopy with circularly polarized X-rays. *Science* **259**, 658 (1993).
- Fischer, P. *et al.* Magnetic domain imaging with a transmission X-ray microscope. *J. Magn. Magn. Mater.* **198–199**, 624–627 (1999).
- Eisebitt, S. *et al.* Lensless imaging of magnetic nanostructures by X-ray spectroholography. *Nature* **432**, 885–888 (2004).
- Boeglin, C. *et al.* Distinguishing the ultrafast dynamics of spin and orbital moments in solids. *Nature* **465**, 458–461 (2010).
- Radu, I. *et al.* Transient ferromagnetic-like state mediating ultrafast reversal of antiferromagnetically coupled spins. *Nature* **472**, 205–208 (2011).
- Beaurepaire, E., Merle, J.-C., Daunois, A. & Bigot, J.-Y. Ultrafast spin dynamics in ferromagnetic nickel. *Phys. Rev. Lett.* **76**, 4250–4253 (1996).
- López-Flores, V. *et al.* Time-resolved X-ray magnetic circular dichroism study of ultrafast demagnetization in a CoPd ferromagnetic film excited by circularly polarized laser pulse. *Phys. Rev. B* **86**, 014424 (2012).
- Graves, C. E. *et al.* Nanoscale spin reversal by non-local angular momentum transfer following ultrafast laser excitation in ferrimagnetic GdFeCo. *Nature Mater.* **12**, 293–298 (2013).
- Popmintchev, T. *et al.* Bright coherent ultrahigh harmonics in the keV X-ray regime from mid-infrared femtosecond lasers. *Science* **336**, 1287–1291 (2012).
- Seaberg, M. D. *et al.* Ultrahigh 22 nm resolution coherent diffractive imaging using a desktop 13 nm high harmonic source. *Opt. Express* **19**, 22470–22479 (2011).
- Kienberger, R. *et al.* Atomic transient recorder. *Nature* **427**, 817–821 (2004).
- Wörner, H. J., Bertrand, J. B., Kartashov, D. V., Corkum, P. B. & Villeneuve, D. M. Following a chemical reaction using high-harmonic interferometry. *Nature* **466**, 604–607 (2010).
- Siemens, M. E. *et al.* Quasi-ballistic thermal transport from nanoscale interfaces observed using ultrafast coherent soft X-ray beams. *Nature Mater.* **9**, 26–30 (2010).
- Li, W. *et al.* Time-resolved dynamics in N₂O₄ probed using high harmonic generation. *Science* **322**, 1207–1211 (2008).
- Sandhu, A. S. *et al.* Observing the creation of electronic Feshbach resonances in soft X-ray-induced O₂ dissociation. *Science* **322**, 1081–1085 (2008).
- Cavalieri, A. L. *et al.* Attosecond spectroscopy in condensed matter. *Nature* **449**, 1029–1032 (2007).
- Salières, P. *et al.* Frequency-domain interferometry in the XUV with high-order harmonics. *Phys. Rev. Lett.* **83**, 5483–5486 (1999).
- La-O-Vorakiat, C. *et al.* Ultrafast demagnetization dynamics at the M edges of magnetic elements observed using a tabletop high-harmonic soft X-ray source. *Phys. Rev. Lett.* **103**, 257402 (2009).
- Mathias, S. *et al.* Probing the timescale of the exchange interaction in a ferromagnetic alloy. *Proc. Natl Acad. Sci. USA* **109**, 4792–4797 (2012).
- Turgut, E. *et al.* Controlling the competition between optically induced ultrafast spin-flip scattering and spin transport in magnetic multilayers. *Phys. Rev. Lett.* **110**, 197201 (2013).
- Corkum, P. B. Plasma perspective on strong field multiphoton ionization. *Phys. Rev. Lett.* **71**, 1994–1997 (1993).
- Möller, M. *et al.* Dependence of high-order-harmonic-generation yield on driving-laser ellipticity. *Phys. Rev. A* **86**, 011401 (2012).
- Weihe, F. A. *et al.* Polarization of high-intensity high-harmonic generation. *Phys. Rev. A* **51**, R3433–R3436 (1995).
- Alon, O. E., Averbukh, V. & Moiseyev, N. Selection rules for the high harmonic generation spectra. *Phys. Rev. Lett.* **80**, 3743–3746 (1998).
- Yuan, K.-J. & Bandrauk, A. D. Circularly polarized molecular high-order harmonic generation in H₂⁺ with intense laser pulses and static fields. *Phys. Rev. A* **83**, 063422 (2011).
- Mauger, F., Bandrauk, A. D., Kamor, A., Uzer, T. & Chandre, C. Quantum-classical correspondence in circularly polarized high harmonic generation. *J. Phys. B Atom. Mol. Opt. Phys.* **47**, 041001 (2014).
- Vodungbo, B. *et al.* Polarization control of high order harmonics in the EUV photon energy range. *Opt. Express* **19**, 4346–4356 (2011).
- Liu, L. Z., O'Keeffe, K. & Hooker, S. M. Optical rotation quasi-phase-matching for circularly polarized high harmonic generation. *Opt. Lett.* **37**, 2415–2417 (2012).
- Fleischer, A., Sidorenko, P. & Cohen, O. Generation of high-order harmonics with controllable elliptical polarization. *Opt. Lett.* **38**, 223–225 (2013).
- Yuan, K.-J. & Bandrauk, A. D. Single circularly polarized attosecond pulse generation by intense few cycle elliptically polarized laser pulses and terahertz fields from molecular media. *Phys. Rev. Lett.* **110**, 023003 (2013).
- Milošević, D. B., Becker, W. & Kopold, R. Generation of circularly polarized high-order harmonics by two-color coplanar field mixing. *Phys. Rev. A* **61**, 063403 (2000).
- Milošević, D. B. & Becker, W. Attosecond pulse trains with unusual nonlinear polarization. *Phys. Rev. A* **62**, 011403 (2000).
- Bandrauk, A. D. & Lu, H. Controlling harmonic generation in molecules with intense laser and static magnetic fields: orientation effects. *Phys. Rev. A* **68**, 043408 (2003).
- Zuo, T. & Bandrauk, A. D. High-order harmonic generation in intense laser and magnetic fields. *J. Nonlinear Opt. Phys. Mater.* **04**, 533–546 (1995).
- Long, S., Becker, W. & McIver, J. K. Model calculations of polarization-dependent two-color high-harmonic generation. *Phys. Rev. A* **52**, 2262–2278 (1995).
- Eichmann, H. *et al.* Polarization-dependent high-order two-color mixing. *Phys. Rev. A* **51**, R3414–R3417 (1995).
- Fleischer, A., Kfir, O., Diskin, T., Sidorenko, P. & Cohen, O. Spin angular momentum and tunable polarization in high-harmonic generation. *Nature Photon.* **8**, 543–549 (2014).
- Cohen, O., Popmintchev, T., Gaudiosi, D. M., Murnane, M. M. & Kapteyn, H. C. Unified microscopic-macroscopic formulation of high-order difference-frequency mixing in plasmas. *Phys. Rev. Lett.* **98**, 043903 (2007).
- Popmintchev, T. *et al.* Phase matching of high harmonic generation in the soft and hard X-ray regions of the spectrum. *Proc. Natl Acad. Sci. USA* **106**, 10516–10521 (2009).
- Oppeneer, P. M. in *Handbook of Magnetic Materials* Vol. 13 (ed. Buschow, K. H. J.) 229–422 (Elsevier, 2001).
- Henke, B. L., Gullikson, E. M. & Davis, J. C. X-ray interactions: photoabsorption, scattering, transmission, and reflection at $E = 50$ –30,000 eV, $Z = 1$ –92. *Atom. Data Nucl. Data Tables* **54**, 181–342 (1993).
- Valencia, S. *et al.* Faraday rotation spectra at shallow core levels: 3p edges of Fe, Co, and Ni. *New J. Phys.* **8**, 254 (2006).
- Xie, X. *et al.* Internal momentum state mapping using high harmonic radiation. *Phys. Rev. Lett.* **101**, 033901 (2008).
- Zeitoun, P. *et al.* High-intensity highly coherent soft X-ray femtosecond laser seeded by a high harmonic beam. *Nature* **431**, 426–429 (2004).

Acknowledgements

This work was supported by the USA–Israel Binational Science Foundation (BSF). The Technion group was supported by the Israel Science Foundation (grant no. 1225/14) and

the Israeli Center of Research Excellence ‘circle of light’ supported by the I-CORE Program of the Planning and Budgeting Committee and The Israel Science Foundation. The experiment was carried out in JILA. O.K. and O.C. acknowledge the warm hospitality in JILA. The JILA and NIST authors acknowledge funding from the US Department of Energy Office of Basic Energy Sciences (award no. DE-SC0002002). JILA also acknowledges funding from the Physics Frontiers Center Program and from an AFOSR DURIP award for the laser system used for this work. P.G. acknowledges support from the Deutsche Forschungsgemeinschaft (no. GR 4234/1-1). R.K. acknowledges the Swedish Research Council (VR) for financial support.

Author contributions

O.C., M.M. and H.K. conceived and supervised the project. O.K., P.G., E.T. and A.F. designed the experimental set-up. O.K., P.G., E.T., R.K., D.Z., T.P. and D.P. constructed the

experimental set-up and conducted the experiment. O.K. and P.G. analysed the data with input from other authors. O.K. developed the theory and carried out the numerical simulations. O.K., P.G. and O.C. wrote the manuscript with input from all other authors.

Additional information

Supplementary information is available in the [online version](#) of the paper. Reprints and permissions information is available online at www.nature.com/reprints. Correspondence and requests for materials should be addressed to O.K. and O.C.

Competing financial interests

The authors declare no competing financial interests.

Generation of bright phase-matched circularly-polarized extreme ultraviolet high harmonics

Ofer Kfir¹, Patrik Grychtol², Emrah Turgut², Ronny Knut^{2,3}, Dmitriy Zusin²,
Dimitar Popmintchev², Tenio Popmintchev², Hans Nembach^{2,3}, Justin M. Shaw³, Avner Fleischer^{1,4},
Henry Kapteyn², Margaret Murnane² and Oren Cohen¹.

¹*Solid State Institute and Physics Department, Technion, Haifa 32000, Israel*

²*Department of Physics and JILA, University of Colorado and NIST, Boulder, CO 80309, USA*

³*Electromagnetics Division, National Institute of Standards and Technology, Boulder, CO 80305, USA*

⁴*Department of Physics and Optical Engineering, Ort Braude College, Karmiel 21982, Israel*

1. Phase matching of circular HHG

Full phase matching of a nonlinear process corresponds to where the coherence length of the process diverges; i.e. when the right hand side of Eq. (3) equals zero. To make this possible, the effective index changes, Δn_1 and Δn_2 , must have opposite sign. Furthermore, only one harmonic order can be fully phase matched for a given effective index ratio of the two colors $\Delta n_2/\Delta n_1$. In order to phase match the harmonic order $q = 3m \pm 1$, the effective index ratio should be -

$$\frac{\Delta n_2}{\Delta n_1} = -\frac{m \pm 1}{2m} \quad (\text{S.1})$$

For example, in order to phase match the 28th or 40th HHG orders, ($m = 9, 13$) and ($\pm \rightarrow +$), the index ratio $\Delta n_2/\Delta n_1$ should be -0.55 or -0.54, respectively.

Explicit representation of the effective index change for each component of the bi-chromatic driver, Δn_1 , Δn_2 is given by¹

$$\Delta n_i = \left(\frac{\lambda_i k_i}{2\pi} - 1 \right) = - \left\{ \left(\frac{u_{11}^2 \lambda_i^2}{8\pi^2 a^2} \right) - P \left[(1 - \eta)(n_i - 1) - \frac{1}{2\pi} \eta N_{atm} r_e \lambda_i^2 \right] \right\} \quad (\text{S.2})$$

Here, $i=1$ for the fundamental and $i=2$ for the second harmonic driver, u_{11} is the modal factor², a is the inner radius of the hollow waveguide, λ_i and k_i are the wavelength and wave-vector of i^{th} field, P is the gas pressure in atmospheres, η is the ionization fraction, r_e is the classical radius of the electron, N_{atm} is the number density of atoms at atmospheric pressure, and n_i is the index of refraction of the gas for wavelength λ_i at atmospheric pressure. The modal term, $u_{11}^2 \lambda_i^2 / 8\pi^2 a^2$, and the plasma term $\eta N_{atm} r_e \lambda_i^2 / 2\pi$, contribute negatively to Δn , mainly to the fundamental driver, λ_1 , while the normal refraction of the neutral gas, $(n_i - 1)$, contributes positively to Δn , mainly to the second harmonic field, λ_2 . Since full phase matching requires that $\Delta n_2/\Delta n_1 < 0$, it is achievable when Δn_1 (long wavelength) is negative and Δn_2 (short wavelength) is positive.

The gas pressure in which high harmonics are generated acts as a continuous knob to control the HHG phase matching. At zero pressure, the effective index ratio is $\Delta n_2 / \Delta n_1 = 1/4$, where both $\Delta n_2, \Delta n_1$ are negative due to modal term, $u_{11}^2 \lambda_i^2 / 8\pi^2 a^2$. Pressurizing the hollow waveguide with a weakly ionized gas contributes positively to Δn_2 , more than to Δn_1 , so high enough gas pressure can make $\Delta n_2 / \Delta n_1 < -0.5$, as required for phase matching of high order harmonics. Tuning the pressure, therefore, selects the HHG order to be phase matched according to Eq. (S.1) and (S.2). However, re-absorption of HHG in the gas reduces the contrast between the optimally phase matched harmonic (e.g. 28th order in Fig. 1b) and other harmonic orders.

Figure S.1 plots the coherence length vs. the absorption length of few HHG orders in Ne for a 1% ionization level. When the ratio of coherence length, L_c , to absorption length, L_a , is above 6 (see dashed line), the HHG flux is 90% of the fully phase matched case, and the emission is effectively phase matched. The low order HHG (19th and 20th) increase at pressures around 100 Torr and are phase matched up to far above 1000 Torr, whereas the high order harmonics (40th and 41st) are phase matched in a narrower pressure range. The pressure dependent spectrograms in Fig. 3c (measured) and Fig. 3d (theory) agree with this description, although the calculation takes into account additional effects, such as the HHG source density (i.e. gas density) and parasitic re-absorption in residual gas downstream from the phase matching region (details below).

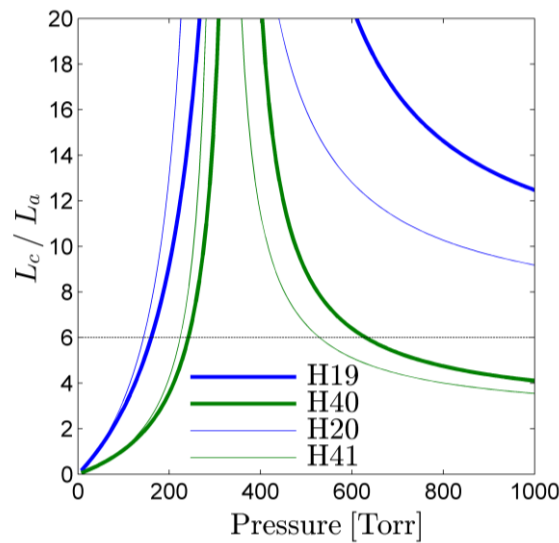


Figure S.1 | (a) The coherence length vs. absorption length of circularly polarized harmonics in a Ne filled hollow waveguide. At $L_c / L_a = 6$ (see dashed black line), the output HHG flux is 90% of the flux under perfect phase matching condition, so the HHG are said to be phase matched. The low order HHG orders (say 19th and 20th) are phase matched from about 100 Torr to above 1000 Torr, whereas the high order harmonics (40th and 41st) are phase matched in a narrower pressure range. The solid and fine lines correspond to HHG of the groups $q = 3m + 1$ and $q = 3m - 1$, respectively. L_c of the 19th order deviates from the 20th due to the helicity selective factor, $\pm \Delta n$, in Eq. (3).

2. Critical ionization for full phase matching of circularly polarized HHG

The critical ionization, η_{cr} , is the ionization fraction above which pressure tuning cannot bring about phase matching of circularly polarized HHG. Specifically, pressure tuning cannot reduce the ratio $\Delta n_2/\Delta n_1$ below -0.5. The value of η_{cr} can be derived from Eq. (S.2) -

$$\eta_{cr} = [2(n_2 - 1) + (n_1 - 1)] \cdot \left\{ 2(n_2 - 1) + (n_1 - 1) + \frac{3}{4\pi} N_{atm} r_e \lambda_1^2 \right\}^{-1} \quad (S.3)$$

This critical ionization differs from critical ionization of HHG driven with single laser field². For HHG driven by one field in a large focus geometry, the critical ionization level is independent of the pressure, and occurs when the dispersion of the neutral atoms and plasma balance each other. (In a waveguide, the value of the critical ionization is reduced slightly below that of a large focal geometry, due to the presence of waveguide dispersion). In contrast, circularly polarized HHG driven by bi-chromatic fields requires that Δn_i is nonzero: Δn_1 should be negative and Δn_2 positive. Since optimal Δn_1 is negative and Δn_2 is positive, η_{cr} is larger for bi-chromatic circular driver, than for HHG driven with the fundamental only, but smaller than HHG driven by the second harmonic only.

3. Numerical procedure for a pressure dependent spectrogram

Simulating the single atom response to the driving bi-chromatic field is the principal step for calculating pressure dependent HHG emission. We approximate the atom as a binding potential and a single, spin-less electron, and solve the Schrödinger equation in three spatial dimensions (3D) and time. The binding potential is an inverted Gaussian given by $V_{atom}(\vec{r}) = -V_0 e^{-s|\vec{r}|^2}$, where $V_0 = 2.38$ and $s = 1/\sqrt{8}$ atomic units (at.u.). The single electron initially occupies the lowest state, having ionization potential of a Ne atom, 0.794 at.u. (21.6 eV). The driving bi-chromatic field, $\vec{E}_{BC}(t)$, induces a linear potential, within the dipole approximation, so overall the potential is $V(\vec{r}, t) = -\vec{E}_{BC}(t) \cdot \vec{r} + V_{atom}(\vec{r})$. Here $\vec{E}_{BC}(t) = \vec{E}_1(t) + \vec{E}_2(t)$, $\vec{E}_1(t) = E_{1,0} e^{-(t/t_p)^6} (-\sin(\omega_0 t) \hat{x} + \cos(\omega_0 t) \hat{y})$ and $\vec{E}_2(t) = E_{2,0} e^{-(t/t_p)^6} (\sin(2\omega_0 t + \phi_2) \hat{x} + \cos(2\omega_0 t + \phi_2) \hat{y})$, where $E_{1,0}$, $E_{2,0}$ correspond to peak intensities of $2.3 \cdot 10^{18} [W/m^2]$ and $2.3 \cdot 10^{18} [W/m^2]$, respectively. t_p , correspond to 15 femtoseconds, $\omega_0 = 0.0577$ is the frequency of 790nm light in atomic units, ϕ_2 is the phase of the second harmonic field relative to the fundamental. \hat{x}, \hat{y} are the Cartesian coordinates unit vectors and \vec{r} is the radius vector. The 6-power Gaussian envelope of the simulated bi-chromatic pulse is chosen to reduce spectral effects originating from variations of the pulse envelope. The emitted HHG field, \vec{E}_{HHG} , is calculated using Ehrenfest theorem, $\vec{E}_{HHG}(t) \propto \langle \psi(t) | \vec{\nabla} V_{atom} | \psi(t) \rangle$, where ψ is the electronic wave function. The proportion constant is not accounted for since it applies globally to the entire radiation spectrum.

The HHG phase strongly depends on the effective index of the bi-chromatic driving field in the gas medium. To account for the phase differences between the fundamental and second harmonic fields, we calculate HHG emission from a single atom 100 times, where each

iteration uses a different phase between the fundamental and second harmonic drivers. The phase for the h^{th} iteration is $\phi_{2,h} = 2\pi h/100$, where $h=1,2,3\dots 100$, and the calculated HHG emission is assigned to an atoms positioned at $z_h = \phi_{2,h}c[2\omega_0(\Delta n_1 - \Delta n_2)]^{-1}$. The effect of the fundamental driver phase velocity is accounted for once the single atom emission, $\vec{E}_{HHG,h}(t)$, is done. Since the fundamental phase velocity in the gas filled waveguide (Eq. (S.2)) differs from free space propagation, it requires additional time, $\Delta n_1 z_h/c$, to reach the atom at z_h . Therefore, the emission at z_h is delayed from the calculated emission, and is given by $\vec{E}_{HHG,h}(t - \Delta n_1 z_h/c)$.

The macroscopic HHG phase matched signal is a coherent sum of the single atom emissions that undergo partial re-absorption in the gas. At the end of the phase matching region, z_{PM} , the HHG intensity is $|\sum_h P \vec{E}_{HHG,h}(t - \Delta n_1 z_h/c) e^{-(z_{PM}-z_h)/L_{abs}}|^2$, where L_{abs} is the absorption length of the HHG in the gas. The gas pressure, P , is inserted to the calculation to account for the density of HHG emitters. Upon exiting the phase matching region, the HHG field can undergo additional parasitic re-absorption in the neutral gas. This is simulated by adding absorption from a $150 \mu m$ layer of the gas at pressure P . The pressure-dependent spectrogram in Fig. 3d is calculated by repeating the above for multiple pressure of Ne gas at an ionization fraction $\eta = 1.2\%$.

4. Dynamics of circularly polarized, counter rotating bi-chromatic field

The polarization of the light field is usually described by its Lissajous curve, that is, the electric field of circular, elliptical, and linear polarization follows a circle, ellipse and a line, respectively. In that sense, the polarization of a circularly polarized, counter rotating bi-chromatic field composed of a fundamental field at 790 nm and its second harmonic has a 3-fold “rosette” shape polarization, as described in Fig. 1a in the text. To better illustrate the dynamical aspect of this rosette polarization we attach a movie showing the fundamental driver (red) second harmonic driver (blue) and the resulting field of the bi-chromatic driver (purple). (See supplementary movie)

5. Calculating and comparing the photon flux of circular and linear polarized harmonics.

To determine the feasibility of future XMCD pump-probe experiments using a source of circularly polarized high harmonics, we have calculated the absolute flux contained in a single circular-polarized harmonic at the Co M -edge below 60 eV and compared it with the flux obtained in previous ultrafast element-selective HHG experiments exploiting the transversal magneto-optical Kerr effect (T-MOKE) in reflection using linear polarized harmonics³⁻⁷. To this end, we have simulated the transmission as well as reflection properties of our EUV beamline components taking into account the efficiency of our CCD camera. Specifically, we have used the RAY simulation software package that is a powerful design tool developed at BESSY for synchrotron radiation beamlines⁸. Moreover, we have calibrated the efficiency of our CCD detector according to the procedure recommended by the manufacturer.

As schematically depicted in Fig. 2 of the main article, the harmonics emerging from our waveguide pass through a 200 nm thick Al filter (with a 5 nm thick Al₂O₃ layer) and the 100 nm thick Co film, which is tilted by 45° with respect to the HHG beam, before entering our spectrometer. The spectrometer consists of a toroid mirror (glass substrate coated by 100 nm of B₄C and tilted at a grazing angle of 8°), a laminar gold grating patterned on top of Si substrate (with a groove density of 500 lines/mm, a groove depth of 20 nm and which is mounted at a grazing angle of 12°), two 200 nm thick Al filter (each of which having a 5 nm thick Al₂O₃ layer) and a CCD camera (Andor – Newton DO-920). As can be seen in Fig. S.2, this combination of components results in a theoretical throughput of 10⁻⁵-10⁻⁴ EUV photons in the vicinity of the Co *M*-edge at 58 eV. This is comparable to the efficiency of previously reported measurements in the T-MOKE geometry.

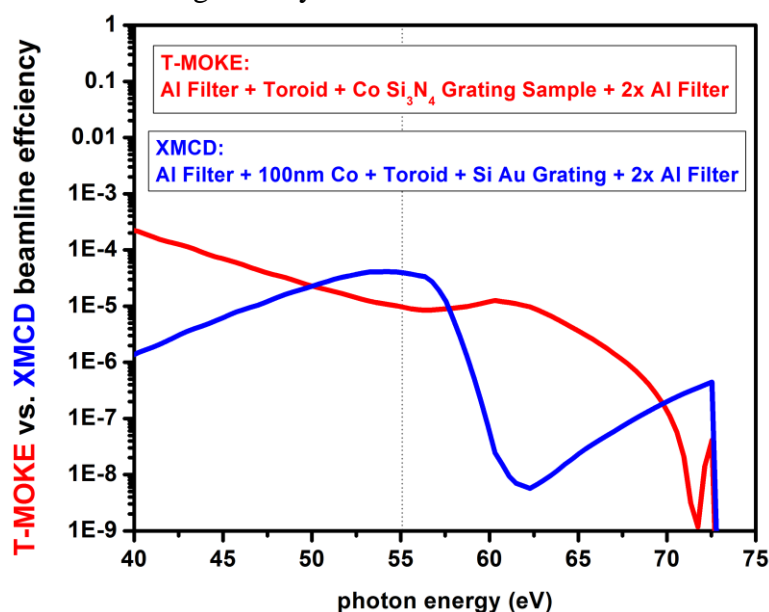


Figure S.2 | Efficiency comparison of T-MOKE and XMCD HHG EUV beamlines

In this spectral region, the CCD chip of the camera has a quantum efficiency of about 30%, *i.e.* about every third photon is absorbed by the back-thinned Si chip. Each absorbed photon with an energy of 55 eV generates approximately 55/3.65 photoelectrons or 55/45.63 counts using the standard gain setting of our camera. Taking into account the simulated efficiency of our XMCD (T-MOKE) beamline of about $4 \cdot 10^{-5}$ ($1.5 \cdot 10^{-5}$) and the fact that we observe around 10^4 counts/s in the 55 eV harmonics of both HHG setups, we obtain a photon flux of approximately $7 \cdot 10^8$ photons/s in a single circular harmonic, which is only 2-3 times smaller than the flux of the very same linear harmonic in our T-MOKE experiment. Considering the very high signal-to-noise ratio that we have already attained in our static XMCD experiment as well as the relatively high effective thickness of our Co sample (140 nm) in comparison to the penetration depth of a laser excitation pulse (a few tens of nm), we conclude that ultrafast pump-probe investigations of chiral phenomena are within the capabilities of our current experimental circular HHG apparatus.

6. Useful features of circular HHG using a counter-rotating bi-chromatic field.

We generate bright circularly polarized harmonics by co-propagating bi-chromatic 790 nm and 395 nm (ω and 2ω) driving laser beams with counter-rotating circular polarization^{9–11}. This approach has several useful properties that are beneficial for applications. First, the conversion efficiency to circularly polarized high harmonics is comparable to the conversion efficiency of traditional HHG, where linearly polarized driving lasers produce linearly polarized high harmonics (see Fig. S.2 in Ref¹¹). Second, the generated spectrum consists only of circularly polarized harmonics. Third, consecutive harmonics exhibit opposite helicity. Fourth, the circular-polarization of the harmonics is manifested in the high harmonic spectrum due to angular momentum conservation rules: thus, it is not essential to directly or continuously monitor their polarization. As explained below, when the bi-chromatic driving lasers consist of the fundamental and second harmonic frequencies, absence of the $3m^{\text{th}}$ harmonics ($m=1,2,3\dots$) indicates that the polarizations of $3m+1$ and $3m-1$ harmonics are circular with helicity that correspond to the polarization of the fundamental and 2^{nd} harmonic fields, respectively. Fifth, the polarization of the generated harmonics is largely insensitive to the intensities and intensity ratio between the bi-chromatic driving lasers. This is an important feature because both the intensity of, and the intensity ratio between, the two driving fields can vary within the focal spot and along the direction of propagation. Also, this feature is important for the robustness of the method to misalignment and instability of the driving fields. Sixth, as shown below, the generation process can be fully phase matched. Finally, the mechanism for producing circularly polarized harmonics in this direct approach is based only on the circular polarization of the driving pulses and is otherwise insensitive with respect to the nonlinear medium and other properties of the driving laser beams. Thus, we expect that many experimental applications that were implemented using linearly polarized HHG can be directly transferred to circularly polarized harmonics. For example, we expect that the use of long-wavelength bi-chromatic driving lasers will extend bright circularly-polarized HHG into the keV region, which will span the water-window region as well as the magnetically sensitive L -shell absorption edges of the 3d ferromagnets¹².

7. Degree of circular polarization

The 4 Stocks parameters¹³ S_0, S_1, S_2, S_3 fully characterize the polarization state of light:

the 0th parameter S_0 measures the overall radiation intensity, S_1 and S_2 measure the degree of linear polarization and its orientation and S_3 , measures the degree of circular polarization and helicity. More accurately, the degree of circular polarization is given by S_3 normalized by the total intensity S_0 and has the form

$$\frac{S_3}{S_0} = \frac{I_R - I_L}{I_R + I_L} \quad (\text{S.4})$$

where I_R is the intensity of the right-rotating circularly-polarized component of the light and I_L is the intensity of the left-rotating circularly-polarized component. Usually one records I_R, I_L by measuring the intensity passing through a polarizer that transmits pure circular polarization with right or left helicity, respectively. Measuring $S_3/S_0 = 1$ indicates pure right-rotating circularly-polarized light (RCP) while measuring $S_3/S_0 = -1$ corresponds to pure left-rotating circularly-polarized light (LCP).

The XMCD measurement that we conducted within this work retrieves the degree of circular polarization in the spectral region where Co is active magneto-optically. Incident light on the Co foil can be decomposed into RCP light of intensity I_R and LCP light of intensity I_L . The light intensity transmitted through the Co sample with “up” or “down” magnetization depends on the MO constant $\Delta\beta$ ¹⁴, the light wave vector \vec{k}_0 and the sample thickness L

$$\begin{aligned} I^{up} &= I_R e^{2|\vec{k}_0|\Delta\beta L} + I_L e^{-2|\vec{k}_0|\Delta\beta L} \\ I^{down} &= I_R e^{-2|\vec{k}_0|\Delta\beta L} + I_L e^{+2|\vec{k}_0|\Delta\beta L}. \end{aligned} \quad (\text{S.5})$$

Substituting eq. S.5 into the definition of the XMCD asymmetry, $= (I^{up} - I^{down}) / (I^{up} + I^{down})$, and using eq. S.4, gives the degree of circular polarization:

$$\frac{S_3}{S_0} = \frac{A}{\tanh(2|\vec{k}_0|\Delta\beta L)}. \quad (\text{S.6})$$

Fig S.3 presents the degree of circularity retrieved from the measured asymmetry. The left rotating HHG orders 31st (48 eV) and 34th (53 eV) are highly circular with $S_3/S_0 = -1.01 \pm 0.15$ and -0.98 ± 0.19 , respectively. That is, within our experimental uncertainty, the polarization is pure LCP! On the other hand, the right rotating HHG orders 32nd (50 eV) and 34th (55 eV) have low degree of circularity, $S_3/S_0 = 0.37 \pm 0.22$ and 0.31 ± 0.10 , respectively. The degree of circularity, S_3/S_0 , cannot be retrieved below 45 eV since $\Delta\beta$ is still unknown¹⁴. Furthermore, at the 37th HHG order (58 eV) the MO coefficient, $\Delta\beta$, nullifies so eq. S.6 diverges and S_3/S_0 cannot be retrieved.

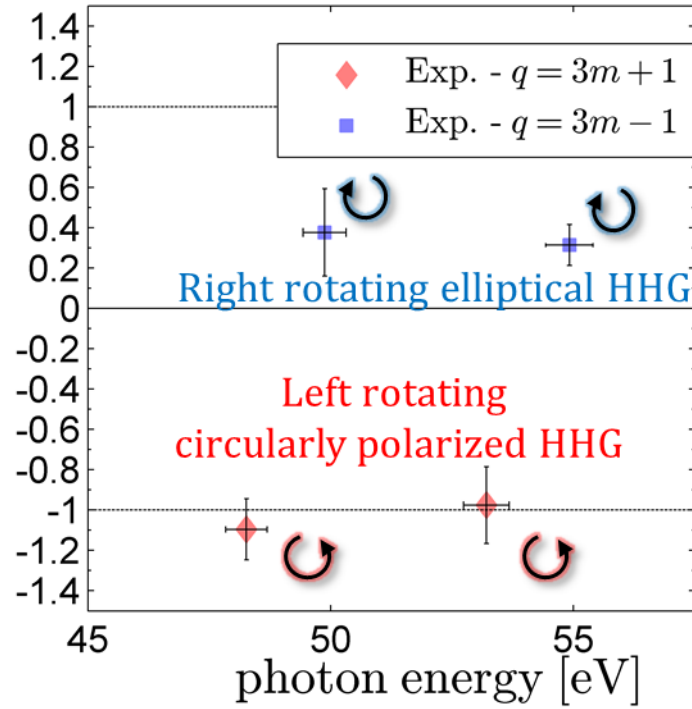


Figure S.3 | Normalized Stocks parameter S_3/S_0 for HHG in the Cobalt M-edge. The magneto optical selectiveness in the M-edge of Co acts essentially as a polarizer for circular polarization. Using the XMCD asymmetry we conclude that HHG orders $q = 3m + 1$ are purely left-rotating circularly polarized (within our experimental uncertainty): $S_3/S_0 = -1.01 \pm 0.15$ for the 31st order (48 eV) and $S_3/S_0 = -0.98 \pm 0.19$ for the 34th order (53 eV). The right rotating HHG orders, $q = 3m - 1$, present low degree of circularity: $S_3/S_0 = 0.37 \pm 0.22$ for the 32nd order (50 eV) and $S_3/S_0 = 0.31 \pm 0.10$ for the 35th order (55 eV). Therefore, the right rotating HHG are elliptical or partially polarized. The degree of circularity and the error bars are calculated from the average and standard deviation of the XMCD asymmetry over each harmonic order divided by $\tanh(2|\vec{k}_0|\Delta\beta L)$ according to eq. S.6.

References:

1. Rundquist, A. *et al.* phase-matched generation of coherent soft X-rays. *Science* **280**, 1412–1415 (1998).
2. Popmintchev, T. *et al.* phase matching of high harmonic generation in the soft and hard X-ray regions of the spectrum. *Proc. Natl. Acad. Sci.* **106**, 10516–10521 (2009).
3. La-O-Vorakiat, C. *et al.* ultrafast demagnetization dynamics at the M edges of magnetic elements observed using a tabletop high-harmonic soft X-ray source. *Phys. Rev. Lett.* **103**, 257402 (2009).

4. La-O-Vorakiat, C. *et al.* ultrafast demagnetization measurements using extreme ultraviolet light: comparison of electronic and magnetic contributions. *Phys. Rev. X* **2**, 011005 (2012).
5. Mathias, S. *et al.* probing the timescale of the exchange interaction in a ferromagnetic alloy. *Proc. Natl. Acad. Sci.* (2012). doi:10.1073/pnas.1201371109
6. Rudolf, D. *et al.* ultrafast magnetization enhancement in metallic multilayers driven by superdiffusive spin current. *Nat. Commun.* **3**, 1037 (2012).
7. Turgut, E. *et al.* controlling the competition between optically induced ultrafast spin-flip scattering and spin transport in magnetic multilayers. *Phys. Rev. Lett.* **110**, 197201 (2013).
8. Schäfers, F. in *Modern Developments in X-Ray and Neutron Optics* (eds. Erko, A., Idir, D. M., Krist, D. T. & Michette, P. A. G.) 9–41 (Springer Berlin Heidelberg, 2008). at http://link.springer.com/chapter/10.1007/978-3-540-74561-7_2
9. Long, S., Becker, W. & McIver, J. K. model calculations of polarization-dependent two-color high-harmonic generation. *Phys. Rev. A* **52**, 2262–2278 (1995).
10. Eichmann, H. *et al.* polarization-dependent high-order two-color mixing. *Phys. Rev. A* **51**, R3414–R3417 (1995).
11. Fleischer, A., Kfir, O., Diskin, T., Sidorenko, P. & Cohen, O. spin angular momentum and tunable polarization in high-harmonic generation. *Nat. Photonics* **8**, 543–549 (2014).
12. Popmintchev, T. *et al.* bright coherent ultrahigh harmonics in the keV X-ray regime from mid-infrared femtosecond lasers. *Science* **336**, 1287–1291 (2012).
13. Hecht, E. *Optics*. (Addison-Wesley, 2002).
14. Valencia, S. *et al.* Faraday rotation spectra at shallow core levels: 3p edges of Fe, Co, and Ni. *New J. Phys.* **8**, 254–254 (2006).